remote sensing

MDPI

Article

Measures of Spatial Autocorrelation Changes in Multitemporal SAR Images for Event Landslides Detection

Alessandro C. Mondini

CNR IRPI, Via Della Madonna Alta 126, 06128 Perugia, Italy; alessandro.mondini@irpi.cnr.it; Tel.: +39-393-107-1838

Academic Editors: Zhong Lu, Chaoying Zhao and Prasad S. Thenkabail
Received: 28 February 2017; Accepted: 29 May 2017; Published: 2 June 2017

Abstract: Landslides cause damages and affect victims worldwide, but landslide information is lacking. Even large events may not leave records when they happen in remote areas or simply do not impact with vulnerable elements. This paper proposes a procedure to measure spatial autocorrelation changes induced by event landslides in a multi-temporal series of synthetic aperture radar (SAR) intensity Sentinel-1 images. The procedure first measures pixel-based changes between consecutive couples of SAR intensity images using the Log-Ratio index, then it follows the temporal evolution of the spatial autocorrelation inside the Log-Ratio layers using the Moran's *I* index and the semivariance. When an event occurs, the Moran's *I* index and the semivariance increase compared to the values measured before and after the event. The spatial autocorrelation growth is due to the local homogenization of the soil response caused by the event landslide. The emerging clusters of autocorrelated pixels generated by the event are localized by a process of optimal segmentation of the log-ratio layers. The procedure was used to intercept an event that occurred in August 2015 in Myanmar, Tozang area, when strong rainfall precipitations triggered a number of landslides. A prognostic use of the method promises to increase the availability of information about the number of events at the regional scale, and to facilitate the production of inventory maps, yielding useful results to study the phenomenon for model tuning, landslide forecast model validation, and the relationship between triggering factors and number of occurred events.

Keywords: spatial autocorrelation; event landslides; SAR intensity

1. Introduction

Landslides can occur anywhere in the world, creating victims, and causing economic losses, and property damage [1]. Despite their importance, landslide information is lacking [2]. In many cases, large events remain unnoticed unless they impact or interact with vulnerable elements. This scarcity of information is critical for the comprehension of the phenomena at a global/continental scale in relationship to triggering events, for landslide modeling, and for landslide forecast models performance validation [3].

A landslide is the movement of a mass of rock, debris, or earth down a slope under the influence of gravity [4]. Landslides can be caused by natural phenomena including earthquakes, rapid snow melting, and intense or prolonged rainfall, or they can be induced by human activities such as timber clearcut or road construction, or a combination of both [5]. A multitude of landslides caused by a single trigger will be called here event landslides [6].

Getting information about landslides occurrences can be hard, especially when they take place in remote areas. Traditionally, landslides are manually detected, interpreted, and mapped through visual interpretation of stereoscopic aerial photography, in some cases aided by field surveys [7,8].

Manual interpretation is usually applied "on demand" because it is time-consuming and expensive, aerial photographs cover small areas and acquisitions, and flyovers revisiting intervals are limited or irregular. Furthermore, remote sites can be difficult and dangerous to access [9]. Consequently, a multitude of events remain unnoticed or unreported.

The large availability of high-resolution satellite data and the development of image processing techniques for event landslide detection and mapping is a potential source to obtain information on slope instabilities over large areas [2,10]. Researchers concentrate most of their effort in the implementation and validation of methods for mapping known event landslides using optical images, or in the use of advanced Differential Interferometric Synthetic Aperture Radar (DInSAR) techniques and Synthetic Aperture Radar (SAR) images for monitoring slow moving landslides [2,11]. On the contrary, the systematic and automatic interception or detection of new event landslides is not a subject of extensive research [11]. This paper wants to investigate the possibility to be informed about the occurrence of an event landslide and eventually, about its potential localization using measures of spatial autocorrelation in a multi-temporal series of SAR images. Zhou et al. [12] proposed a method to detect anomalies in regions caused by floods using autocorrelation analysis of multi-temporal series of optical satellite images. In this work, the framework proposed in [12] is modified and adapted for the use of SAR images and applied to measure the effects of an event landslide that occurred in Chin Division, Myanmar, triggered in July 2015 by strong rainfalls.

SAR amplitude/intensity images can be used to detect and map changes in the land surface cover [13,14]. Changes can be caused by natural events, including floods [15], natural fires [16], and earthquakes [17]. SAR amplitude/intensity images are occasionally used to map single landslides at slope scale [18] but not exploited at event (catchment) scale [11]. Problems and obstacles in their use are represented by a complex pre-processing, the acquisition geometry that can affect the quality of the images over mountainous areas where landslides are likely to occur, a certain difficulty in using the SAR signal in traditional statistical classification approaches (mainly due to speckling) [19], and perhaps a certain attitude against using this kind of product in the landslide mapping community. Land surface cover changes occurring between two images acquired over the same area but in different times can be measured through some pixel-by-pixel image comparison carried out by difference, or by a ratio operator to reduce the speckling effect typical in SAR images [13,14,20,21]. When event landslides occur in previously vegetated areas, they usually remove the vegetation to leave the soil bare or partially bare. Vegetated and bare surfaces have different properties (e.g., roughness, the dielectric value of the backscattering material), and then the backscattered waves amplitudes recorded by the pre- and post-event SAR images can change, helping to detect landslides [18,22].

Spatial autocorrelation is the correlation among values of a single variable strictly attributable to their relatively close locational positions on a two-dimensional surface [23]. Spatial autocorrelation prevails in virtually all georeferenced data [24], and it is widely used in Remote Sensing for information extraction [25–27], for landslide susceptibility [28] and hazard modeling [29]. The method to measure changes of spatial autocorrelation proposed in this work is based on the analysis of the temporal evolution of the Moran's I index [23], and semivariance measure [25,27] applied to the Log-Ratio (LR) layers obtained coupling consecutive SAR intensity images. In the study areas, the two indexes showed a quite constant behavior in the LR layers obtained coupling images before the event (LR-pre) or images after the event (LR-post) and a consistent increase in the LR layer when pre- and post-event images were coupled (LR-between). The increase was due to land cover changes caused by the event landslides that gave origin to clusters of pixels with similar values, raising the level of spatial autocorrelation in the layer. The positioning of areas of changes candidate to be landslides was obtained through a process based on a digital image segment optimization [30] adapted for landslide mapping [10]. The new clusters recognized by the optimal segmentation all lay in areas of changes due to landslides, independently mapped through a Support Vector Machine classification of a pre- and a post-event optical Rapid Eye images.

The landslide event occurred in Myanmar in 2015 introduced enough changes in the land cover to result in a measurable change in spatial autocorrelation inside SAR images. This information was used to assess when and where the event occurred and it can be preparatory for a prognostic use of the procedure for new event landslide detection. This work aims at showing a way to increase the availability of information on landslide events otherwise unnoticed starting from an unused point of view: it advices for the occurrence of an event in between two consecutive images measuring a global change and for its location finding local changes in the post-event image.

Other techniques can be then addressed to produce inventory maps [2,11,31]. More frequent information on landslide occurrence promises to facilitate the validation of landslide forecast models at catchment scale that do not require the production of an inventory (i.e., threshold-based at catchment/slope unit scale) [32], and to better understand landslide phenomena at a global scale in relation to triggering factors.

The paper is organized as follows. In Section 2, the test case, the event, data availability, and relative pre-processing are introduced. In Section 3, the proposed method is presented in mathematical terms, together with the results obtained in the study. Results are discussed in Section 4. In Section 5, the lesson learned is summarized.

2. Test Case

2.1. Study Area and Event Description

The study area is located in Chin Division, Myanmar (Figure 1) where exceptional rainfall triggered a large number of landslides in late July 2015, including the giant Tonzang landslide (Figure 2). It is preliminary delimited by the available Sentinel-1 images swath (around 2597356w, 719663s, 2716753e, 504281n in EPSG 32646 WGS84 UTM zone 46 projection) and further refined by the analysis and by the coverage of RapidEye images later procured (around 571500w, 2591500s, 596500e, 2640500n in EPSG 32646 WGS84 UTM zone 46 projection) .

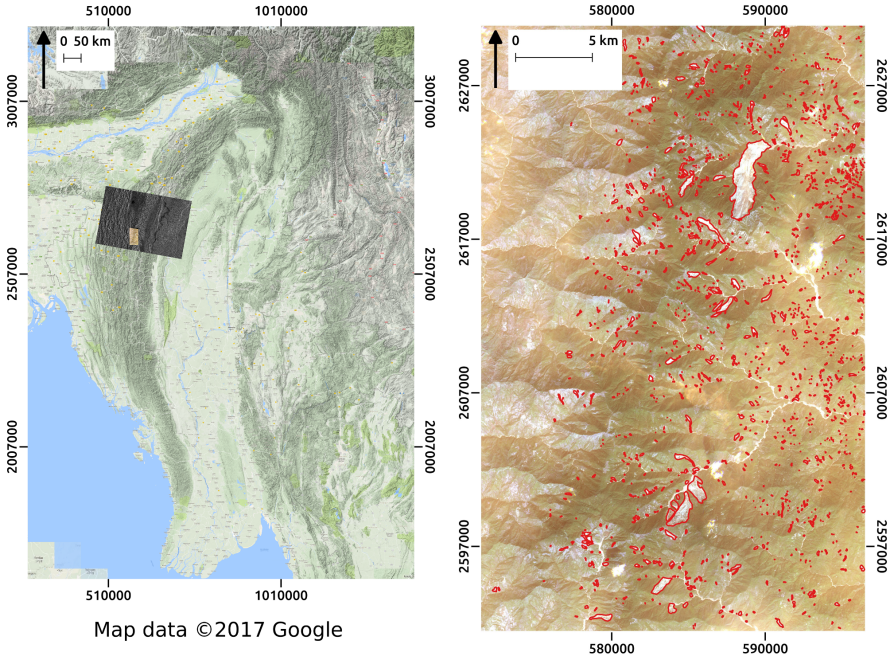

Figure 1. Study areas location and the event landslide map. On the left: overlapped with the Google physical map, the study areas delimited by the available Sentinel-1 (black and white) and Rapid-Eye (colored) images. It is located in northern Myanmar, Chin division. On the right: the event landslide inventory map obtained through the Support Vector Machine overlapped to the post-event Rapid-Eye.

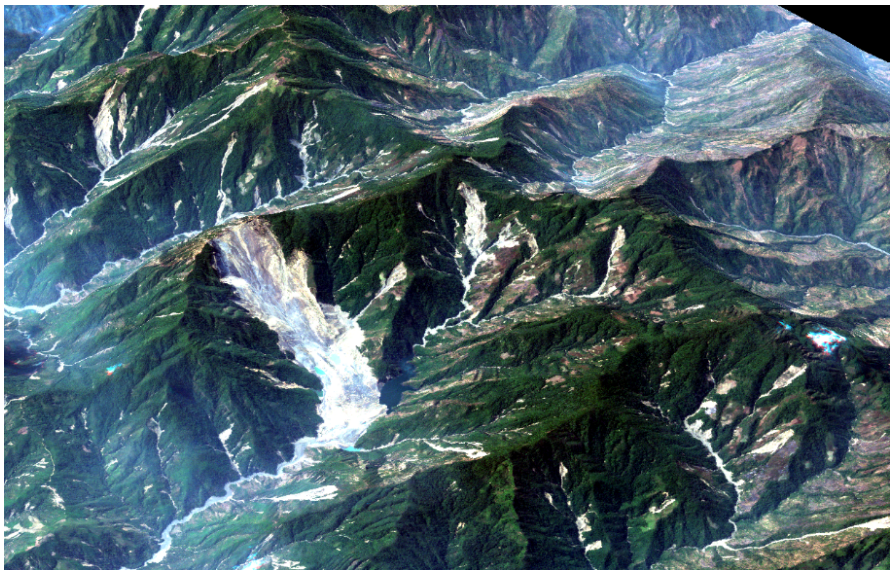

Figure 2. The Giant Tonzang landslide. The picture was obtained overlapping the post event RapidEye image to the available Digital Elevation Model.

According to the ASTER Digital Elevation Model (DEM) at 30 m [33], elevation ranges 2363 m from 328 to 2691 m with a mean value of 1411 m. Slope ranges 64.5 degrees from 0 to 64.5 degrees and has a mean value of 25.6 degrees. Many natural watercourses flow among mountain ranges running from north to south, forming valleys and gorges. Land is mainly covered by tropical forest with spots of bare soil on the north-west part caused probably by recent fires, antecedent the event. Chin State is sparsely populated. A succession of sub vertical sub parallel layers of metasedimentary and sedimentary rocks from Jurassic to Cretaceous assemble the geology of the study area [34]. The "Myanmar post-disaster needs assessment of floods and landslides July–September 2015" report compiled by the Government of the Republic of the Union of Myanmar [35] states that the Myanmar's climate is largely tropical with three seasons: the monsoon/rainy season (May–October), cold season (November–February), and hot season (March–April). Rainfall during the monsoon season totals more than 500 cm in upper Myanmar.

Myanmar is exposed to a range of natural hazards, including floods, cyclones, earthquakes, landslides, and tsunamis. Within the last seven days of July 2015, over 30 percent more rain fell than in any other month over the past 25 years [35]. In July and August 2015, widespread floods and landslides affecting 12 out of the 14 states in Myanmar displaced 1,676,086 people and caused 132 fatalities. They destroyed public and private infrastructure, including houses, railways, roads, bridges, schools, health facilities, and monasteries, and had extensive impacts on the agriculture sector. Unprecedented extreme rainfalls caused landslides in the Chin State in particular in remote areas difficult to access [35], peculiar was the reactivation of a large, old, and deep-seated landslide on which as a detailed geologic and geo-engineering study revealed parts of Hakha had been built (Figure 2) [36]. The just described event is the only one occurred the period covered by the multi-temporal series of available SAR images.

2.2. Available Data and Pre-Processing

Sixteen Sentinel-1A SAR images were downloaded from the Sentinel Scientific Data Hub [37] in Level-1 Ground Range Detected (GRD) high-resolution (HR) format (GRDH), with VV-VH polarizations and Interferometric Wide (IW) acquisition mode. GRDH images are already multi-looked with a number of looks with a pixel spacing in range and azimuth of 10 m [38]. GRDH images only include amplitude and related intensity bands in digital numbers (DN) for each polarization. Images were acquired in descending relative orbit 4 from 17 October 2014 to 27 May 2016 with irregular acquisition intervals due to the ramp-up phase of the satellite. In the period from June 2015

to November 2015 no images were made available. For each single SAR image, first, the precise orbit was downloaded and applied, then the thermal noise was removed. Intensity digital pixel values were converted in radiometric calibrated backscatter σ_0. All the images were then singularly co-registered to a master (the first acquired image of the available series) using a DEM-assisted procedure. Images were later filtered for speckling reduction using the adaptive Frost filter with a filter size in X and Y of three pixels, and a damping factor of two [39]. The LR index layer was then computed in every pixel for each couple of VV polarization and VH polarization consecutive images (Figure 3) using the following formula:

$$LR = ln(\frac{\sigma_{0,i}}{\sigma_{0,i-1}}), \quad (1)$$

where i is the image index with i ranging from 2 to the number of images, ln the natural logarithm. Every single LR layer was later projected and ortho-rectified in UTM WGS84 using a DEM. Pixels in layover or in shadows (around 0.1% over the entire Sentinel-1 scenes) were masked. All the just-described steps were carried out using SNAP 5.0 (the free software provided by the the European Space Agency under the Scientific Exploitation of Operational Missions framework), and all the pre-processing steps involving a DEM (including layover and shadows masking) used the Shuttle Radar Topography Mission (SRTM) 3Sec DEM directly auto-downloaded from the SNAP software.

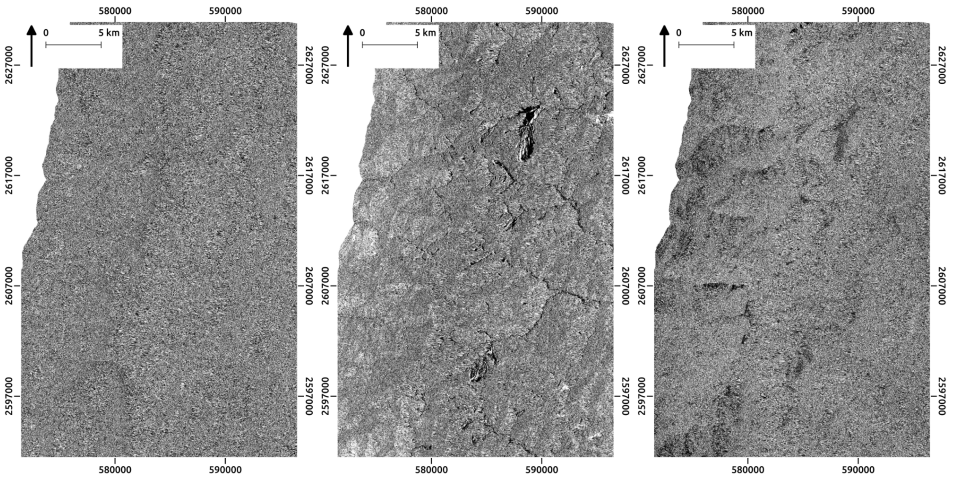

Figure 3. Examples of Log-Ratio (LR) layers. Left: the LR layer obtained using the last two pre-event synthetic aperture radar (SAR) images (LR-pre). Middle: the LR layer obtained using the last pre- and the first post-event SAR images (LR-between). Right: the LR layer obtained using the first two post-event SAR images (LR-post).

Two pre-event optical RapidEye images acquired on 9 March 2015, and two post-event RapidEye acquired on 18 February 2016 were later obtained and used to contextualize the analysis and to obtain the map of changes (including landslides) as ancillary data. Images were obtained with a 3A pre-processing level, which includes radiometric and geometric corrections. All RapidEye images were first atmospheric corrected using the Fast Line-of-sight Atmospheric Analysis of Hypercubes (FLAASH) module available in ENVI Software [40]. The two post-event and the two pre-event images were respectively mosaicked to obtain a unique post-event scene and a unique pre-event scene. The relative geometric co-registration between the pre- and post-event scenes was checked using 30 homologous pixels in each scene, and the overall mis-registration error resulted smaller than the pixel size. Unfortunately, very few pixels (seven) were found in mountainous areas. Like in Mondini et al. [9], the Normalized Differential Vegetation Index change, the Spectral Angle, and the fourth principal component (the most correlated to the previous indexes) between the pre- and post-event images were obtained and stacked to get a multi-layer composition of changes. The stack of changes was successively classified using a Support Vector Machine trained with five training areas in regions that

experienced changes, and 10 training areas in areas which apparently did not experience changes. The final map is a binary changes/no-changes map. About 97% of the area resulted unchanged, while the remaining 3% was mostly ascribable to the presence of new landslides including their runouts (93%) and sparse deposits of debris along the rivers (7%). Rivers were removed manually.

3. Method and Results

The flow chart of the procedure is shown in Figure 4. The method first measures the spatial autocorrelation in a temporal series of LR layer using global or local spatial statistics including Moran's *I* index and semivariance *S*. When some measures deviate from reference values, an anomaly caused by a change is expected, and eventually identified. The event is further localized using a segmentation process.

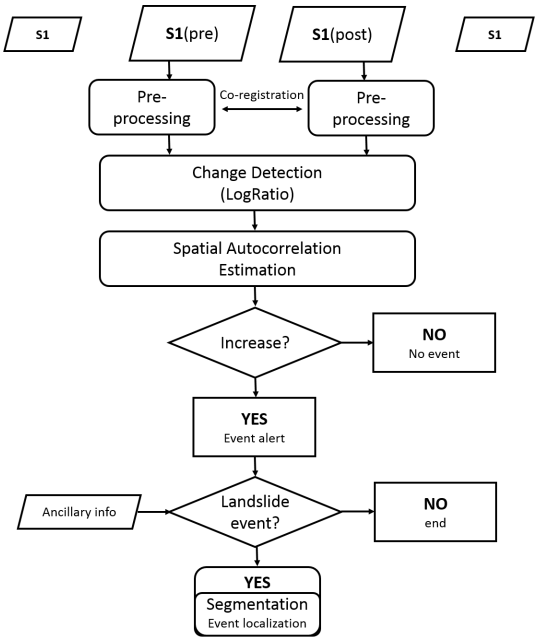

Figure 4. Procedure flow chart. Pre- and Post- are two consecutive Sentinel-1 images. The spatial autocorrelation analysis can be done at different scales, depending on the situation. If the test results positive, then the event is captured, and further localized through the segmentation process.

The Moran's *I* index compares the differences between neighboring pixels to the standard deviation to provide a measure of local homogeneity. It ranges between $+1$ and -1, where $+1$ is strong spatial autocorrelation, 0 spatially uncorrelated data, and -1 strong negative spatial autocorrelation [41]. *I* is calculated in ENVI as follows [23]:

$$I = \frac{\sum_{i=1}^{n}\sum_{j=1}^{n} c_{ij}(y_i - \overline{y}_i)(y_j - \overline{y}_j) / \sum_{i=1}^{n}\sum_{j=1}^{n} c_{ij}}{\frac{\sum_{i=1}^{n}(y_i - \overline{y}_i)^2}{n}}, \quad (2)$$

where n is the number of spatial units (pixels) indexed by i and j, y is the value of the LR index in each pixel, $\overline{y}$ the mean of y, and c_{ij} are elements of the spatial weight matrix C that is assigned through the definition of the neighborhood rule that defines which adjacent pixels to compare to the central pixel. Weights are 1 for adjacent pixels and 0 otherwise. The index can also be estimated at a defined lag distance of pixels. The semivariance *S* measures the dissimilarity within a dataset through the squared difference between neighboring pixels' values (Equation (3)):

$$S = \frac{1}{2}\frac{1}{n}\sum_{i=1}^{n}(y_{i+h}) - yi)^2, \quad (3)$$

where h is the value of the maximum lag of pixels.

In this work, the I index was preliminary computed for all the layers over the entire scene of the GRDH Sentinel-1 images (25,360 samples, 16,632 lines) adopting the "Queen's" rule which takes into account the eight neighboring pixels, and with a maximum lag of 30 pixels. The LR-between layer showed higher values of spatial autocorrelation than in all the LR-pre and LR-post layers in both the polarizations and for all lags (e.g., $I = 0.136$ for the last pre-event layer, $I = 0.225$ in between the event, and $I = 0.160$ for the first post-event layer at a lag distance of five pixels, for the VH polarization).

Only in the LR-between layer, I was also computed inside 5000 × 5000 and 2000 × 2000 pixel moving windows scanning the whole layer with horizontal and vertical steps of 1000 pixels.

In at least four local areas, the screening showed values of I higher than the values obtained in the LR-pre, and LR-post layers, with an increase ranging from about 50% to the maximum of about 1000% depending on the window size and the area covered by the window. Maximum gap was experienced for 2000 × 2000 pixel windows with $\Delta I = 0.53$ ($I_{min} = 0.06$, $I_{max} = 0.59$). Three local areas are situated in flat regions along rivers (yellow boxes in Figure 5) and they show signs left by floods (water in the pre-event image and no water in the post-event) with a strong LR signal, or flooded areas (green boxes in Figure 5) with low values of LR. In the fourth local area, which is situated in a mountainous region, the event landslide was visually recognized. The three areas with floods show an increase of I in general higher than the area with landslides.

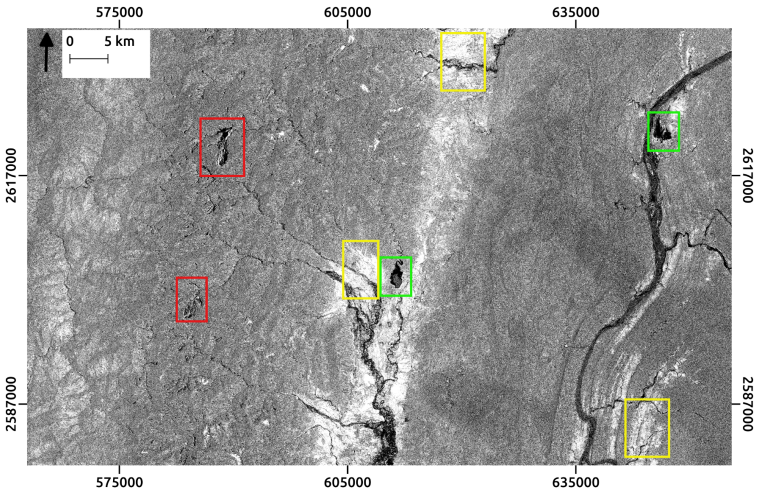

Figure 5. Log-Ratio (LR)-between layer in part of the Sentinel-1 swath. The yellow squares show areas with signs probably left by recent floods, the green current flooded areas, and in red event landslides. Squares here do not coincide with moving windows.

A more detailed analysis was conducted over the area covered by the GeoEye images (Figure 1) selected to overlap as much as possible the windows where an increase of spatial correlation caused by landslides was experienced. The correlograms of I and S, with a maximum lag distance of 30 pixels and obtained using again the "Queen's" rule, for the VH polarization layers are shown in the top of Figure 6. Further analyses were conducted masking in the images the areas where the three biggest landslides (the Tozang landslide, with a total area of 6,302,634 m^2, the second and the third both about 1/4 of the Tozang landslide side) are. The correlograms are shown in the bottom of Figure 6. The latter has the purpose of simulating a much smaller event.

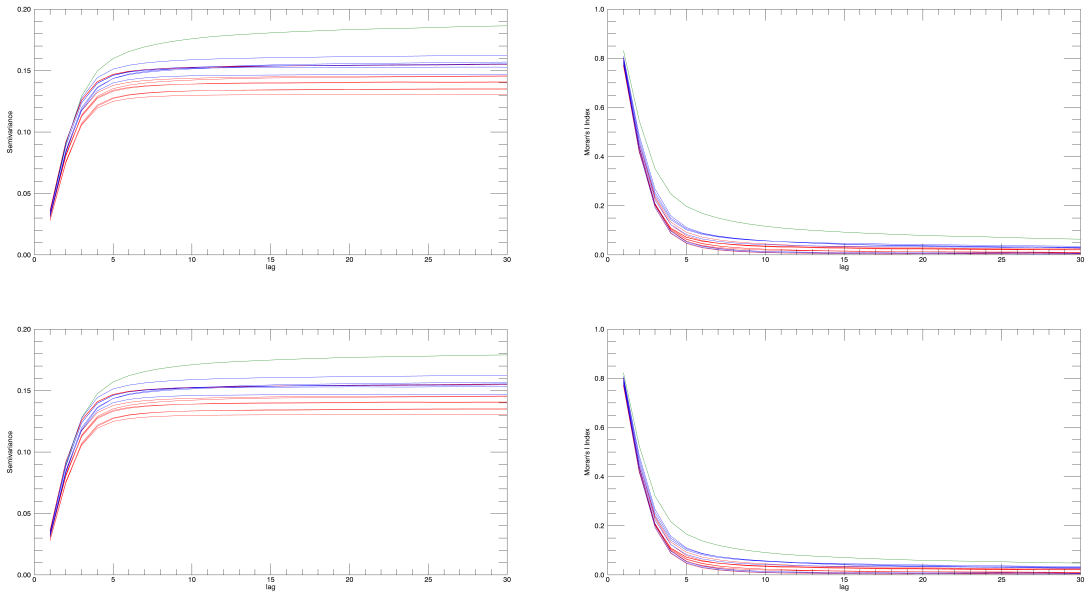

Figure 6. Correlograms for the Moran's *I* index and the semivariance with maximum lag = 30 for all the LR layers, VH channel. For all figures, in red, pre-event curves/values, in blue, post-event curves/values, and in green the curves linked to the event. Top-left: semivariance correlograms of the complete analysis. Bottom-left: semivariance correlograms excluding the three biggest landslides. Top-right Moran's *I* index correlograms of the complete analysis. Bottom-right Moran's *I* index correlograms excluding the three biggest landslides.

Green curves in Figure 6 represent the *I* and *S* correlograms for the LR layer of the event (LR-between), while blue curves and red curves respectively the pre-LR and post-LR layers. Blue and red curves group together defining standard values of spatial autocorrelation inside the layers far from the event, while the green curve shows an occurred change. Values of *I* and *S* are very stable before the event (maximum gap of 0.05 at a lag of 7 pixels for *I* and of 0.03 at lags of pixels higher than 10 for *S*). Immediately after the event, *I* and *S* are higher of few percents and they decrease till the pre-event values after few months.

As an example, in the VH polarization LR layers, obtained using the last two pre-event SAR images (LR-pre), the last pre- and the first post-event SAR images (LR-between), and the first two post-event SAR images (LR-post), *I* assumes values, respectively, of 0.056, 0.197, and 0.102 at a lag distance of five pixels. The corresponding values for the VV polarization LR layers, are 0.070, 0.160, and 0.987. At least in this test case, the change in the index is more evident in VH polarization than in VV polarization.

LR-pre, LR-between, and LR-post layers, clipped by the area defined by the RapidEye images, were segmented to locate clusters of pixels with eventually high spatial autocorrelation. Segmentation allows an image to be partitioned (in this case the LR layers) into regions of interconnected pixels. Using the segmentation module available in ENVI, it is possible to extract segments only, without performing rule-based or example-based classification [42]. The segmentation process is based on a "watershed algorithm" which sorts pixels by increasing gray scale value, then begins with the minimum pixels and "floods" the image, partitioning the image into basins (regions with similar pixel intensities) based on the computed watersheds [43]. Segmentation results depend on a set of parameters, including Intensity level for feature detection, adjust the merging scale level using any Lambda schedule, and the kernel dimension [42]. Using a simplified single scale version of the procedure proposed by Martha et al. [10] for landslide detection optimal segmentation, the best set of parameters for segmentation was obtained for the three VH and VV polarization LR layers.

The procedure proposed by Martha et al. [10] wants to minimize the under- and over-segmentation through an iterative process of parameters selection to maximize an objective function.

$$F(v, I) = f(v) + f(I)\,, \tag{4}$$

where $f(v)$ and $f(I)$ are the normalization functions of the intra-segment variance and v the Moran's I index of the segments obtained with a set of defined parameters. Fixing the kernel dimension at three, the two-dimensional space of the Intensity/Lambda parameters space values both ranging from 0 to 1 or 0 to 100 percent was scanned with steps of 0.1. The intensity and Lambda parameters that optimize the segmentation are (0.2;0.2), (0.2;0.5), and (0.2;0.4), respectively for LR-pre, LR-between, and LR-post for the VH polarization. Some measures of the obtained segments are reported in Table 1. In the LR-pre (Figure 3), there is a dominant salt-and-pepper behavior consequence of speckles in the original images and no evidence of emerging clusters (Figure 7). Compared to the LR-pre, the LR-between layer (Figure 3) shows a reduction of the number of the segments and the presence of much larger segments (Figure 7). Percentile values shown in Table 1 confirm an increase of the clusters size in the LR-between layer. Overlapping the segmentation to the classification obtained using the optical images, all segments with area larger than the average area from the bulk (95th percentile of the LR-pre layer) lie or intersect regions classified as changes, and they cover about 65% percent of the class. LR-post (Figure 3) layer segmentation shows an intermediate condition. The position of the emerging clusters represents a potential localization of the event landslides.

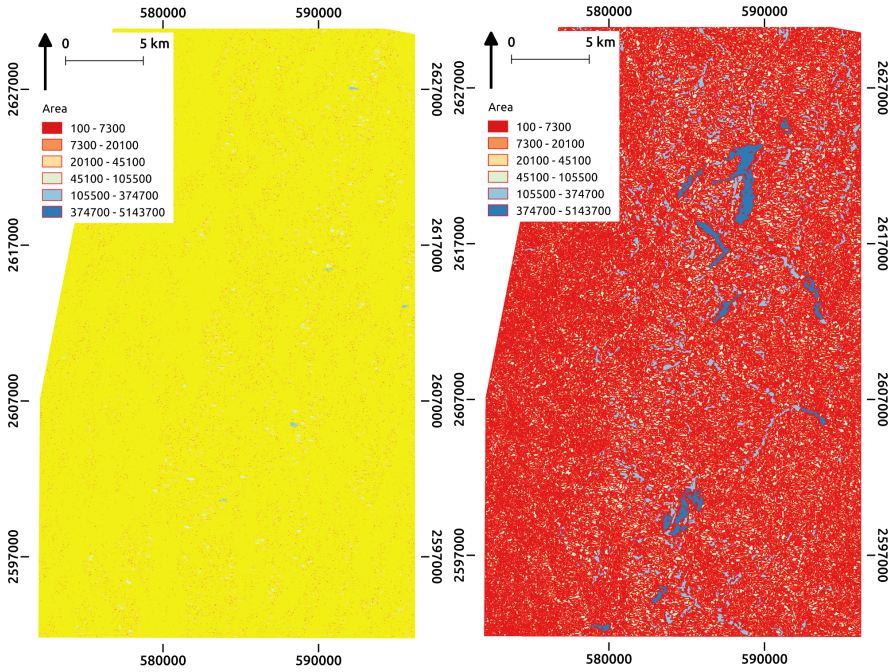

Figure 7. Optimal segmentation results for the VH layers. (**Left**) the optimal segmentation obtained for the LR-pre. (**Right**) the optimal segmentation obtained for the LR-between. The scale for the LR-between was obtained using the "natural breaks" function available in Qgis to maximize the variance between individual classes and least variance within each class. The scale of the LR-pre was adapted according to the LR-between scale.

Table 1. Segments properties values obtained using the optimal segmentation

	Pre	Between	Post
Number	221,066	120,654	226,885
Max area (m^2)	165,600	5,143,700	570,900
Min area (m^2)	100	100	100
Intensity	0.2	0.2	0.1
Lambda	0.2	0.5	0.3
50th percentile	800	3300	2300
95th percentile	3800	27,400	20,600
99.9th percentile	25,300	113,569	50,500

Starting from the 95th percentile (Table 1), clusters in the in-between layer size larger than all clusters found in the pre-event layers and indicate where to look for the localization of the event.

The optimal segmentation applied to the VV polarization still shows the capacity to locate the event but with a lower number of big clusters in particular in the 95th percentile (24,300) and in the 99.9th percentile (98,561), confirming the lower spatial autocorrelation compared to the VH channel.

4. Discussion

In this work, the possibility of detecting an event landslide using multi-temporal SAR intensity satellite images and spatial autocorrelation measures was investigated and verified. In the period covered by the series of the available Sentinel-1 dual-polarization SAR images, fifteen layers of land cover changes for each polarizations were obtained.

In the pre-event (8) and post-event (6) layers the spatial autocorrelation measured using the Moran's I index and semivariance S is almost constant.

In correspondence of the event, the autocorrelation typically doubles. A smaller event was simulated removing from the analysis the areas where the tree largest landslides occurred and the general behavior was confirmed.

The process that changed the radar backscatter between the pre- and the post-event images is ascribable to the changes of the land cover structure, roughness at the wavelength scale of the C band, and the change of the land dielectric constant (moisture content) in the passage from dense canopy to bare soil [13,19] caused by event landslides. In addition, the local incident angle can change the backscattering coefficient, but in this case it is not an issue, assumed to be almost constant in the used temporal stack of images acquired with the same relative orbit and using a ratio-based index. Even if the entire process is not investigated from a physical point of view, in this study, the VH polarization showed more sensitivity to changes probably due the depolarization effects over the vegetation and the post-event rough surface left by the event landslides. Nevertheless, VV polarization still showed enough sensitivity to intercept the event suggesting for an exportability of the method in areas where only VV polarization images are available.

The pre-processing can also influence the extraction of the information from SAR images. Being that the GRDH images are already multi-looked, filtering is probably the most delicate point. The adaptive Frost filter was chosen to smooth the noise in the single radar images because it is able to account for the local properties of the terrain backscatter and is particularly adapt to work in mountainous environments [44]. Parameters were chosen to spatially restrict the action and preserve local discontinuity features in case of landslide presence. In this work, the salt-and-pepper effect in the LR layers far from the event, which is due to the incomplete remotion of the speckles in the images and is seen as highly-structured changed areas, helps to highlight the appearance of new and more homogeneous zones caused by event landslides. Also the use of a pre-event DEM could introduce some local errors in the pre-processing of the post-event SAR images, in particular, in correspondence of very big landslides when layovering and shadows masks are obtained, and in the ortho-rectification step. The statistical approach used in this procedure should mitigate the impact of local problems of

ortho-rectification [45]. Potential but not ascertained errors in masking should be limited to the three big landslides that certainly changed the pre-existing orography. The use of good quality post-event DEMs would be in some circumstances desirable even if barely achievable just after an event.

The increase of spatial autocorrelation in the changes occurred in the larger scene in between the event (partially represented in Figure 5) is caused by more effects, the event landslides, and some floods. In this case, *I* does not provide unique information about landslides but it alerts that some changed have occurred. More effective and resolutive was the analysis at windows level that recognized areas with different levels (low and high) of spatial autocorrelation. Compared to floods, landslides usually give rise to smaller, more disperse changes and with a more heterogeneous signal. Windows covered by floods typically showed higher values of spatial autocorrelation, but in this work different causes of changes were distinguished a posteriori by visual interpretation of the shape and by contextualizing the changes, ascribable in mountainous areas to landslides, or in proximity of rivers to floods. Since only one event landslide is present in the entire scene, this work does not give numerical, systematic and direct evidence that changes triggered by different phenomena (including landslides, floods, and fires) at catchment scale can be automatically distinguished. More experiments must be conducted in terms of window size and ways of moving the window in relationship to different events. Contextual and ancillary information related to the environment, the susceptibility to the events of the area, and the different spectral responses in the images are information that can be used to link a change to its cause.

In the area covered by the available optical images, the change in spatial autocorrelation is caused by the event landslides. The *I* and *S* curves (Figure 6 for the VH polarization) show spatial autocorrelation values at different lags of pixels quite constant in correspondence of the LR layers obtained before and after the event, and a dramatic increase in the layer that measures changes between the two last pre- and first post-event images of the multi-temporal stack (answering when the event occurred). The *I* and *S* changes advise for an occurred land cover change which is small and estimated from the inventory obtained from the optical images of about 3% of the study area and about 2.1% excluding the three largest landslides that account for more than 30% of the affected area. After the event, considering the entire database of landslides, *I* and *S* showed a progressive decrease reaching at the end of the used temporal series values typically shown before the event. This can be an indication of a persisting but decreasing superficial activity of the land inside the large landslides. Excluding the three largest landslides, the temporal behavior of *I* and *S* before and after the event is nearly identical.

I and *S* don't give information on where changes have potentially occurred. The formation of clusters responsible for the increase of the spatial autocorrelation in the LR-between is trapped segmenting the LR layers (answering where to look for). The segmentation procedure was laborious and demanding, but it guaranteed that the parameters Intensity and Full Lambda Schedule used to obtain the final segments were good statistical indicators of optical image segmentation [10]. They minimized the overall intra-segment variance (high similarity of the pixels response inside the segment) and the inter-segment correlation (heterogeneity among the pixels values inside the segment compared to the surrounding segments pixels values), giving the sampling step of 0.1 in the Intensity/Full Lambda Schedule domain. A more dense sampling was not considered, because around the best values of Intensity and Lambda that maximized the *F* function (Equation (4)), *F* typically showed a plateau and resulting segmentations were very similar. The texture kernel size was kept constant and low a priori to avoid introducing further filters and because it was suitable in areas with higher variance [42]. Different geographical contexts and pixel resolutions might require customized choices. For the VH polarization, the final segmentation of the LR-between layer of the event shows an increase of 2500 m^2 in the 50th percentile, of 19,600 m^2 in the 95th percentile, and of 88,269 m^2 in the 99.9th percentile of the segments areas as an indication of a dramatic growth of the spatial autocorrelation in the LR-between compared to the LR-pre. Those clusters address potential event landslides locations. Percentile values can change according to different boundary conditions including, geo-settings of the affected area, and intensity of the triggering hazard. In the test case presented

here, they all lie in or intersect with areas where changes occurred due to landslides. This confirmed that the increase of the autocorrelation value in the LR layer over the event was a consequence of the new landslides. Similar behavior was obtained using VV polarization. In this study, the LR-between optimal segmentation is not enough to get a complete or qualitatively good landslide inventory map. Large segments (from 95th percentile) tend to correctly overlap large landslides of about 70% or 80%, depending on the cases. In general, landslides are covered by more than one segment, and the capacity to recognize segments associated with landslides decreases with the decreasing of the landslide size. This behavior can be ascribable to the different ability to intercept heterogeneities into the two different spectral ranges (optical and SAR). Since the implementation of the formula is complex and the time to scan the space of the parameters (Intensity and Lambda) required a lot of time, the suggested procedure considers first the use of the spatial autocorrelation functions to identify among many pairs of images when an event has occurred (the LR-between), and then to carry out the optimal segmentation only over the selected LR-between, eventually, the final inventory map can be obtained using other strategies [2,11].

In this study, Sentinel-1 GRDH images were not available for about 6 months in between the event. The last pre-event was acquired in June around one and half months before the event, and the first post-event image in November, around four months after the event. Now the frequency acquisition of Sentinel-1 is constant over the area, allowing for a continuous monitoring at high temporal and spatial resolution. The future deployment of this work in other areas is also desirable to assess the reproducibility of the procedure in different geo-environmental contexts. Minimum requirement for the application of the same analysis in other areas is the availability of at least a DEM for pre-processing purposes, and a set of Sentinel-1 images acquired before a potential event. In this study, the variability of the spatial autocorrelation in the pre-event layers resulted very low (below 10%) making possible to assess the reference values of the pre-event status using the first four or five images of the series, there is no evidence that the same number of images would be enough in other areas, in particular in environments where seasonal effects are stronger. Ancillary data like conceptual DEM based susceptibility maps [46], can help in the a-priori characterization of the event. Furthermore, the analysis was primarily set up to ascertain that an event landslide can cause measurable spatial autocorrelation changes. Results allowed a posteriori to correctly identify the layer, among fifteen for each polarization, that traps the event. The correct labeling of the layers suggests for a prognostic use of the procedure to trap future events. From this perspective, more test cases will be helpful to implement a validation strategy and improve the success rate of the entire framework.

5. Conclusions

Over an area of about 42,200 km^2 including the Chin district in Myanmar, where an event landslide triggered by strong rainfalls occurred in July 2015, a multi-temporal series of fifteen log-ratio index layers measuring land cover changes between consecutive Sentinel-1 SAR images from October 2014 to May 2016 was obtained.

Far from the event, spatial autocorrelation inside the log-ratio index layers estimated using the Moran's *I* index and the semivariance showed values nearly constant over the entire scene covered by the Sentinel-1 images and in smaller moving windows of 5000 $\times$ 5000 and 2000 $\times$ 2000 pixels. In correspondence of the event, the autocorrelation increased. In some moving windows, the increase was due to the presence of landslides, in others, it was caused by floods triggered by the same rainfall. In this work, floods caused an increase of spatial autocorrelation, locally higher than the increase caused by landslides but the two natural events were distinguished visually considering the different shapes of the changes and their locations (mountainous areas for landslides and in proximity of rivers for floods).

In a subset of the Sentinel-1 frame covered by a couple of available RapidEye images and including the event landslide, a more detailed analysis was conducted. the Moran's *I* index and the semivariance doubled in the log-ratio index layer intercepting the event. In the layer, event landslides gave origin

to clusters of pixels with similar values, while in stable areas, and in pre-event layers, a salt and pepper effect was predominant. Clusters originated by the event landslides resulted larger in size than clusters found in stable areas and in all pre-event layers using an optimal segmentation process. These clusters intersect landslides mapped using the optical images but they are not enough to obtain an inventory map.

In future, research can address the question if the size of the change of the spatial autocorrelation can be used to know a priori the type of event without any visual interpretation. This can be obtained applying the procedure in more and different contexts. One of the characteristics of the framework is its high level of automation: the method can be deployed at regional scale and run where SAR images are acquired systematically, facilitating the possibility of better discriminating the events, and increasing the availability of spatial and temporal information about landslides, which is particularly important where future climate conditions are expected to raise the frequency and the intensity of landslide occurrence.

Acknowledgments: This research is an outcome of the project Commons (http://www.seom-commonsproject.net/) financed by the European Space Agency under the Scientific Exploitation of Operational Missions (SEOM) framework. Contract n. CLS-DAR-CR-14-234. I am grateful to Malcom Davidson (project P.I) from ESA for his constructive and contributive comments. I am also grateful to the MDPI service for the professional English Editing and to the anonymous Reviewers for their constructive comments.

Conflicts of Interest: Author declares no conflict of interest.

References

1. Petley, D. Global patterns of loss of life from landslides. *Geology* **2012**, *40*, 927–930.
2. Guzzetti, F.; Mondini, A.C.; Cardinali, M.; Fiorucci, F.; Santangelo, M.; Chang, K.T. Landslide inventory maps: New tools for an old problem. *Earth-Sci. Rev.* **2012**, *112*, 42–66.
3. Rossi, M.; Guzzetti, F.; Reichenbach, P.; Mondini, A.C.; Peruccacci, S. Optimal landslide susceptibility zonation based on multiple forecasts. *Geomorphology* **2010**, *114*, 129–142.
4. Cruden, D.; Varnes, D. Landslide types and processes. In *Landslides, Investigation and Mitigation, Special Report 247*; Turner, A., Schuster, R., Eds.; Transportation Research Board: Washington, DC, USA, 1996; pp. 36–75.
5. Aleotti, P.; Chowdhury, R. Landslide hazard assessment: Summary review and new perspectives. *Bull. Eng. Geol. Environ.* **1999**, *58*, 21–44.
6. Guzzetti, F.; Cardinali, M.; Reichenbach, P.; Cipolla, F.; Sebastiani, C.; Galli, M.; Salvati, P. Landslides triggered by the 23 November 2000 rainfall event in the Imperia Province, Western Liguria, Italy. *Eng. Geol.* **2004**, *73*, 229–245.
7. Casale, R.; Margottini, C. (Eds.) The recognition of landslides. In *Floods and Landslides: Integrated Risk Assessment*; Springer: Berlin/Heidelberg, Germany, 1999; pp. 39–44.
8. Saba, S.B.; van der Meijde, M.; van der Werff, H. Spatiotemporal landslide detection for the 2005 Kashmir earthquake region. *Geomorphology* **2010**, *124*, 17–25.
9. Mondini, A.C.; Chang, K.-T.; Yin, H.-Y. Combining multiple change detection indices for mapping landslides triggered by typhoons. *Geomorphology* **2011**, *134*, 440–451.
10. Martha, T.R.; Kerle, N.; van Westen, C.J.; Jetten, V.; Kumar, K.V. Segment Optimization and Data-Driven Thresholding for Knowledge-Based Landslide Detection by Object-Based Image Analysis. *IEEE Trans. Geosci. Remote Sens.* **2011**, *49*, 4928–4943.
11. Casagli, N.; Frodella, W.; Morelli, S.; Tofani, V.; Ciampalini, A.; Intrieri, E.; Raspini, F.; Rossi, G.; Tanteri, L.; Lu, P. Spaceborne, UAV and ground-based remote sensing techniques for landslide mapping, monitoring and early warning. *Geoenviron. Disasters* **2017**, *4*, doi:10.1186/s40677-017-0073-1.
12. Zhou, Z.G.; Tang, P.; Zhou, M. Detecting anomaly regions in satellite image time series based on seasonal autocorrelation analysis. *ISPRS Ann. Photogramm. Remote Sens. Spat. Inf. Sci.* **2016**, *III-3*, 303–310.
13. Bovolo, F.; Bruzzone, L. A detail-preserving scale-driven approach to change detection in multitemporal SAR images. *IEEE Trans. Geosci. Remote Sens.* **2005**, *43*, 2963–2972.
14. Bazi, Y.; Bruzzone, L.; Melgani, F. An unsupervised approach based on the generalized Gaussian model to automatic change detection in multitemporal SAR images. *IEEE Trans. Geosci. Remote Sens.* **2005**, *43*, 874–887.

15. Oberstadler, R.; Hönsch, H.; Huth, D. Assessment of the mapping capabilities of ERS-1 SAR data for flood mapping: A case study in Germany. *Hydrol. Process.* **1997**, *11*, 1415–1425.
16. Jenkins, L.K.; Bourgeau-Chavez, L.L.; French, N.H.F.; Loboda, T.V.; Thelen, B.J. Development of Methods for Detection and Monitoring of Fire Disturbance in the Alaskan Tundra Using a Two-Decade Long Record of Synthetic Aperture Radar Satellite Images. *Remote Sens.* **2014**, *6*, 6347–6364.
17. Gamba, P.; Dell'Acqua, F.; Lisini, G. Change Detection of Multitemporal SAR Data in Urban Areas Combining Feature-Based and Pixel-Based Techniques. *IEEE Trans. Geosci. Remote Sens.* **2006**, *44*, 2820–2827.
18. Raspini, F.; Ciampalini, A.; Del Conte, S.; Lombardi, L.; Nocentini, M.; Gigli, G.; Ferretti, A.; Casagli, N. Exploitation of Amplitude and Phase of Satellite SAR Images for Landslide Mapping: The Case of Montescaglioso (South Italy). *Remote Sens.* **2015**, *7*, 14576–14596.
19. Oliver, C.; Quegan, S. *Understanding Synthetic Aperture Radar Images*; SciTech Radar and Defense Series; SciTech Publishing, Inc.: Raleigh, NC, 2004.
20. Bazi, Y.; Bruzzone, L.; Melgani, F. Automatic identification of the number and values of decision thresholds in the log-ratio image for change detection in SAR images. *IEEE Geosci. Remote Sens. Lett.* **2006**, *3*, 349–353.
21. Richards, J. *Remote Sensing with Imaging Radar, Signals and Communication Technology*; Springer: Berlin/Heidelberg, Germany, 2009; p. 361.
22. Jin, Y.Q.; Wang, D. Automatic Detection of Terrain Surface Changes after Wenchuan Earthquake, May 2008, from ALOS SAR Images Using 2EM-MRF Method. *IEEE Geosci. Remote Sens. Lett.* **2009**, *6*, 344–348.
23. Griffith, D.A. Spatial autocorrelation. In *A Primer*; Association of American Geographers: Washington, DC, USA, 1987.
24. Griffith, D.A.; Chun, Y. Spatial Autocorrelation and Uncertainty Associated with Remotely-Sensed Data. *Remote Sens.* **2016**, *8*, 535.
25. Curran, P.J. The semivariogram in remote sensing: An introduction. *Remote Sens. Environ.* **1988**, *24*, 493–507.
26. Warner, T.A.; Shank, M.C. Spatial autocorrelation analysis of hyperspectral imagery for feature selection. *Remote Sens. Environ.* **1997**, *60*, 58–70.
27. Woodcock, C.E.; Strahler, A.H.; Jupp, D.L. The use of variograms in remote sensing: I. Scene models and simulated images. *Remote Sens. Environ.* **1988**, *25*, 323–348.
28. Lee, S. Application of logistic regression model and its validation for landslide susceptibility mapping using GIS and remote sensing data. *Int. J. Remote Sens.* **2005**, *26*, 1477–1491.
29. Pardeshi, S.D.; Autade, S.E.; Pardeshi, S.S. Landslide hazard assessment: Recent trends and techniques. *SpringerPlus* **2013**, *2*, 523.
30. Espindola, G.; Camara, G.; Reis, I.; Bins, L.; Monteiro, A. Parameter selection for region-growing image segmentation algorithms using spatial autocorrelation. *Int. J. Remote Sens.* **2006**, *14*, 3035–3040.
31. Oliveira, S.C.; Zêzere, J.L.; Catalão, J.; Nico, G. The contribution of PSInSAR interferometry to landslide hazard in weak rock-dominated areas. *Landslides* **2015**, *12*, 703–719.
32. Rossi, M.; Marchesini, I.; Tonelli, G.; Perucacci, S.; Brunetti, M.; Luciani, S.; Ardizzone, F.; Balducci, V.; Bianchi, C.; Cardinali, M.; et al. PPT-tool 2.039-1.1 Italian National Landslide Warning System. In *ICL Landslide Teaching Tools*; Sassa, K., He, B., McSaveney, M., Nagai, O., Eds.; ICL & UNESCO: Paris, France, 2013; pp. 358–358.
33. Global Data Explorer. Available online: https://gdex.cr.usgs.gov/gdex/ (accessed on 31 May 2017).
34. Search OneGeology Datasets. Available online: http://portal.onegeology.org/OnegeologyGlobal (accessed on 31 May 2017).
35. Myanmar—Post-Disaster Needs Assessment of Floods and Landslides: July–September 2015. Available online: http://documents.worldbank.org/curated/en/646661467990966084/Myanmar-Post-disaster-needs-assessment-of-floods-and-landslides-July-September-2015 (accessed on 31 May 2017). (In English)
36. Oo, K.L.; Zaw, K.; Meffre, S.; Myitta; Aung, D.W.; Lai, C.K. Provenance of the Eocene sandstones in the southern Chindwin Basin, Myanmar: Implications for the unroofing history of the Cretaceous–Eocene magmatic arc. *J. Asian Earth Sci.* **2015**, *107*, 172–194.
37. Copernicus Open Access Hub. Available online: https://scihub.copernicus.eu/dhus/#/home (accessed on 31 May 2017).
38. Level-1 Ground Range Detected. Available online: https://sentinel.esa.int/web/sentinel/user-guides/sentinel-1-sar/resolutions/level-1-ground-range-detected (accessed on 31 May 2017).

39. Frost, V.S.; Stiles, J.A.; Shanmugan, K.S.; Holtzman, J.C. A Model for Radar Images and Its Application to Adaptive Digital Filtering of Multiplicative Noise. *IEEE Trans. Pattern Anal. Mach. Intell.* **1982**, *PAMI-4*, 157–166.
40. Fast Line-of-Sight Atmospheric Analysis of Hypercubes (FLAASH). Available online: https://www.harrisgeospatial.com/docs/FLAASH.html (accessed on 31 May 2017).
41. Global Spatial Statistics. Available online: http://www.harrisgeospatial.com/docs/GlobalSpatialStatistics.html (accessed on 31 May 2017).
42. Extract Segments Only. Available online: http://www.harrisgeospatial.com/docs/SegmentOnly.html (accessed on 31 May 2017).
43. Jin, X. Segmentation-Based Image Processing System. US Patent 8,260,048, 4 September 2012.
44. Schellenberger, T.; Ventura, B.; Zebisch, M.; Notarnicola, C. Wet Snow Cover Mapping Algorithm Based on Multitemporal COSMO-SkyMed X-Band SAR Images. *IEEE J. Sel. Top. Appl. Earth Obs. Remote Sens.* **2012**, *5*, 1045–1053.
45. Mondini, A.C.; Viero, A.; Cavalli, M.; Marchi, L.; Herrera, G.; Guzzetti, F. Comparison of event landslide inventories: The Pogliaschina catchment test case, Italy. *Nat. Hazards Earth Syst. Sci.* **2014**, *14*, 1749–1759.
46. Marchesini, I.; Ardizzone, F.; Alvioli, M.; Rossi, M.; Guzzetti, F. Non-susceptible landslide areas in Italy and in the Mediterranean region. *Nat. Hazards Earth Syst. Sci.* **2014**, *14*, 2215–2231.